Local and bulk ^{13}C hyperpolarization in NV-centered diamonds at variable fields and orientations

Gonzalo A. Álvarez,[1,*] Christian O. Bretschneider,[1,*] Ran Fischer,[2,*] Paz London,[2] Hisao Kanda,[3] Shinobu Onoda,[4] Junichi Isoya,[5] David Gershoni,[2] and Lucio Frydman[1,†]

[1] *Department of Chemical Physics, Weizmann Institute of Science, Rehovot, 76100, Israel*
[2] *Department of Physics, Technion, Israel Institute of Technology, Haifa, 32000, Israel*
[3] *National Institute for Materials Science, 1-1 Namiki, Tsukuba, Ibaraki 305-0044, Japan*
[4] *Japan Atomic Energy Agency, 1233 Watanuki, Takasaki, Gunma 370-1292, Japan*
[5] *Research Center for Knowledge Communities, University of Tsukuba, 1- 2 Kasuga, Tsukuba, Ibaraki 305-8550, Japan*

arXiv:1412.8635v1 [quant-ph] 30 Dec 2014

Polarizing nuclear spins is of fundamental importance in biology, chemistry and physics. Methods for hyperpolarizing ^{13}C nuclei from free electrons in bulk, usually demand operation at cryogenic temperatures. Room-temperature approaches targeting diamonds with nitrogen-vacancy (NV) centers could alleviate this need, but hitherto proposed strategies lack generality as they demand stringent conditions on the strength and/or alignment of the magnetic field. We report here an approach for achieving efficient electron→^{13}C spin alignment transfers, compatible with a broad range of magnetic field strengths and field orientations with respect to the diamond crystal. This versatility results from combining coherent microwave- and incoherent laser-induced transitions between selected energy states of the coupled electron-nuclear spin manifold. ^{13}C-detected Nuclear Magnetic Resonance (NMR) experiments demonstrate that this hyperpolarization can be transferred via first-shell or via distant ^{13}Cs, throughout the nuclear bulk ensemble. This method opens new perspectives for applications of diamond NV centers in NMR, and in quantum information processing.

Nuclear spins are the central actors in NMR and magnetic resonance imaging (MRI) [1, 2]. They are also promising vehicles for storing and manipulating quantum information, thanks to their long relaxation times [3, 4]. At room temperature, however, nuclear polarization is very weak, resulting in severe limitations in these spins' applicability. Dynamic nuclear polarization (DNP) [5–7] can bypass these limitations by transferring spin polarization from electrons to nuclei, yet for this process to be efficient cryogenic temperature operations are usually required [8–10]. Electronic spins of NV centers are promising alternatives for polarizing nuclear spins in single crystal diamonds at room temperature conditions [11–14]. Hitherto proposed electron→nuclear polarization transfer methods, however, have so far demanded finely tuned energy matching conditions, such as the field strength and its orientation with respect to the diamond crystal, in order to perform efficiently. These prerequisites pose an obstacle for utilizing these methods in generic applications, including the use of diamond powders in MRI or NMR-based analyses. It is hereby shown that these demands for achieving a robust electron→nuclear polarization transfer can be relaxed by the inclusion of incoherent processes [15, 16]. The method hereby proposed includes a continuous microwave (MW) irradiation that coherently addresses the $0 \leftrightarrow -1$ (or $+1$) $S = 1$ electronic spin transition, while exploiting the asymmetry of the electron-nucleus hyperfine interaction [17–20]. This selective MW addressing is combined with the incoherent spin repopulation effects introduced by the optical pumping process [21, 22], to produce an imbalance between the populations of the coupled nuclear spins. This achievement of steady-state ^{13}C polarization is here demonstrated over a range of magnetic field strengths and orientations as well as of electron-nuclear hyperfine interactions, both in optical studies of single NV-centers and in shuttled NMR measurements of bulk samples. Moreover, by exploiting the versatility of this new approach, we shed light on the minor roles played by hyperfine-imposed spin-diffusion barriers in the achievement of bulk nuclear spin hyperpolarization.

RESULTS

The MW-driven, relaxation-aided polarization transfer scheme. Figure 1a defines the relevant system and active interactions that will be used to introduce our polarization transfer proposal. The system involves a single NV $S = 1$ spin exhibiting a ground-state zero-field splitting $D_0 = 2.87$ GHz. This electronic spin is coupled to nearby or distant ^{13}C nuclear spins ($I = 1/2$) through hyperfine (HF) interactions, and can be optically pumped to populate the electronic $m_s = 0$ level [21, 22]. The application of a weak static magnetic field ($\gamma_e B_0 \ll D_0$), induces an additional splitting of the electronic/nuclear states, leading to the energy level diagram in Fig. 1b. Our scenario assumes a selective MW irradiation that solely addresses the electron $|0\rangle \leftrightarrow |-1\rangle$ spin transitions, allowing one to treat the system as a four-level manifold (Fig. 1b). The nuclear spin components of the eigenstates associated with $m_s = 0$ ($|\beta_\uparrow\rangle$ and $|\beta_\downarrow\rangle$) and $m_s = -1$ ($|\alpha_\uparrow\rangle$ and $|\alpha_\downarrow\rangle$) have different quantization axes, due to the asymmetry imposed by a hyperfine inter-

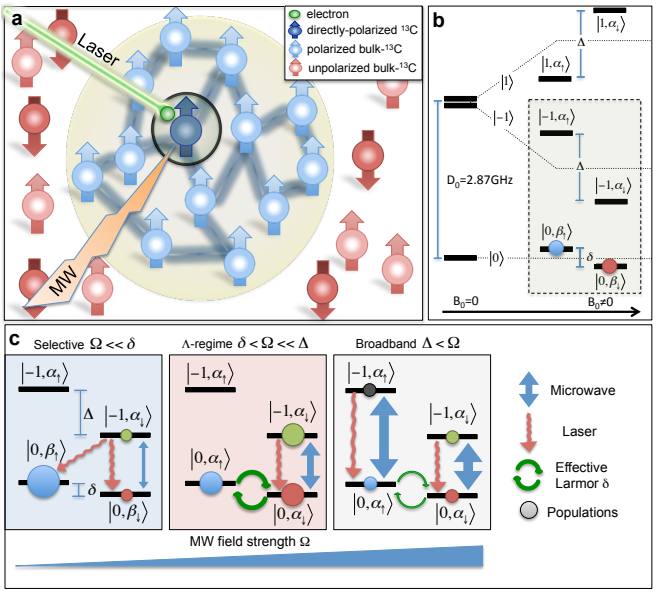

Figure 1. **MW-driven ^{13}C polarization derived from optically-pumped NV centers**. (**a**) Spin-1 NV electronic defect strongly coupled to a ^{13}C nucleus (black circle), irradiated simultaneously by microwave and laser fields. The optically pumped NV-spin transfers its polarization to the coupled nucleus, and eventually to the remaining ^{13}C (the bulk) by interactions within a dipolar spin-network. (**b**) Energy level diagram of the electron defect, HF-coupled to a ^{13}C in presence of a potential magnetic field B_0 (without MW fields). The dashed box shows the energy levels addressed, and stresses an initial state containing equal populations on the lower $|0,\beta_\downarrow\rangle$, $|0,\beta_\uparrow\rangle$ eigenstates after optical pumping. (**c**) Spin dynamical regimes determined by the relation between the MW power and the energy splittings. The solid black lines only represent the eigenstates $|0,\beta_\downarrow\rangle$, $|0,\beta_\uparrow\rangle$, $|-1,\alpha_\downarrow\rangle$ and $|-1,\alpha_\uparrow\rangle$ of the system in the "selective regime"; in the remaining cases these lines represent states $|0,\alpha_\downarrow\rangle$, $|0,\alpha_\uparrow\rangle$, $|-1,\alpha_\downarrow\rangle$ and $|-1,\alpha_\uparrow\rangle$ that are relevant for the MW selection rules, but where $|0,\alpha_\downarrow\rangle$ and $|0,\alpha_\uparrow\rangle$ are linear superpositions of the eigenstates $|0,\beta_\downarrow\rangle$ and $|0,\beta_\uparrow\rangle$. Blue vertical arrows represent the MW excitation, circular green arrows represent an effective Larmor precession with frequency δ, while curly red arrows represent a laser-induced relaxation-like process conserving the nuclear spin state but driving the incoherent $|-1,\alpha_\downarrow\rangle \rightarrow |0,\alpha_\downarrow\rangle$ optical pumping [23]. The filled and colored circles schematize the populations of each state resulting from these dynamics.

action that is absent if the electron state is $m_s = 0$ and present if $m_s = -1$ [17–20]. The corresponding eigenenergies exhibit splittings δ and Δ for the 0 and -1 manifolds, respectively. These differences in level splitting and in quantization axes among nuclear spins that are initially unpolarized, are here exploited to hyperpolarize them. Although not explicitly shown in these energy level diagrams, the electronic and nuclear spins involved in these manifolds are also coupled by dipole-dipole interactions to the ^{13}C ensemble via a spin-coupling network, enabling further polarization transfers to the bulk (Fig. 1a).

Different polarization transfer routes can be activated by irradiating this HF-coupled system, that we discriminate depending on the relative MW field strength Ω vis-a-vis the energy splittings δ and Δ. In the selective $\Omega \ll \delta, \Delta$ regime (Fig. 1c), the MW-induced transitions involve solely two directly-addressed eigenstates. Therefore the population of a third, non-addressed state associated with the $m_S = 0$ manifold, grows systematically as driven by the laser-induced relaxation processes. This generates an imbalance between the $|0,\beta_\downarrow\rangle$ and $|0,\beta_\uparrow\rangle$ populations, equivalent to a nuclear polarization whose direction is defined by $m_s = 0$. As the MW power increases a "$\Lambda-$regime" where transitions are induced among three eigenstates [20], is reached (Fig. 1c). We describe this $\delta \lesssim \Omega \ll \Delta$ regime in a basis set $\{|0,\alpha_\uparrow\rangle, |0,\alpha_\downarrow\rangle, |-1,\alpha_\downarrow\rangle\}$; here $|0,\alpha_\uparrow\rangle$ is a "dark state" for the MW in the sense that $\langle 0,\alpha_\uparrow| S_x |-1,\alpha_\downarrow\rangle = 0$, and $|0,\alpha_\downarrow\rangle$ is a "bright state" $\langle 0,\alpha_\downarrow| S_x |-1,\alpha_\downarrow\rangle = 1$ that is addressed by the MW. Due to the different HF properties associated with $m_s = 0$ and $m_s = -1$, $|-1,\alpha_\downarrow\rangle$ is an eigenstate but $|0,\alpha_\uparrow\rangle$ and $|0,\alpha_\downarrow\rangle$ are not, and therefore oscillate into one another at an effective nuclear Larmor frequency δ. The combined action of this nuclear precession, the MW irradiation and the laser-driven relaxation, results in a redistribution of the initial populations over the three-level system, biasing the "bright" nuclear state population, over its "dark" counterpart. For the example in Fig. 1c, a net nuclear magnetization pointing along the $|\alpha_\downarrow\rangle$ nuclear quantization axis, defined at weak fields by the hyperfine coupling to $m_s = -1$, is then obtained. Finally, as the MW power is further increased, a broadband regime where the electron state is flipped without regards to the nuclear spin state is reached; in such instance no nuclear polarization enrichment is predicted.

Nuclear hyperpolarization in the vicinity of the NV-center. To demonstrate these features, the local ^{13}C polarization achieved via this HF-mediated polarization transfer was probed by optically detected magnetic resonance experiments on a single NV center coupled to a first-shell ^{13}C nuclear spin, characterized by a strong HF coupling $\Delta \approx 130$ MHz [17, 20]. ^{13}C polarization was measured on a crystal lattice rotated on purpose away from the external magnetic field by arbitrary azimuthal and polar angles. The electron spin state was initialized to the $m_s = 0$ state by laser light, and simultaneously irradiated with MWs for 30 μs. The eigenstate populations were then optically measured as a function of the MW frequency ω over a range covering the various eigenstate transitions frequencies (Fig. 2). Two MW powers were used in these experiments, corresponding to the selective and Λ-regimes shown in Fig. 1. For the selective regime a ^{13}C hyperpolarization pointing along the $|\beta_\uparrow\rangle$ or $|\beta_\downarrow\rangle$ directions defined by the $m_s = 0$ eigenstate manifold is reached, depending on the MW irradiation frequency. For the $\Lambda-$regime nuclear hyperpo-

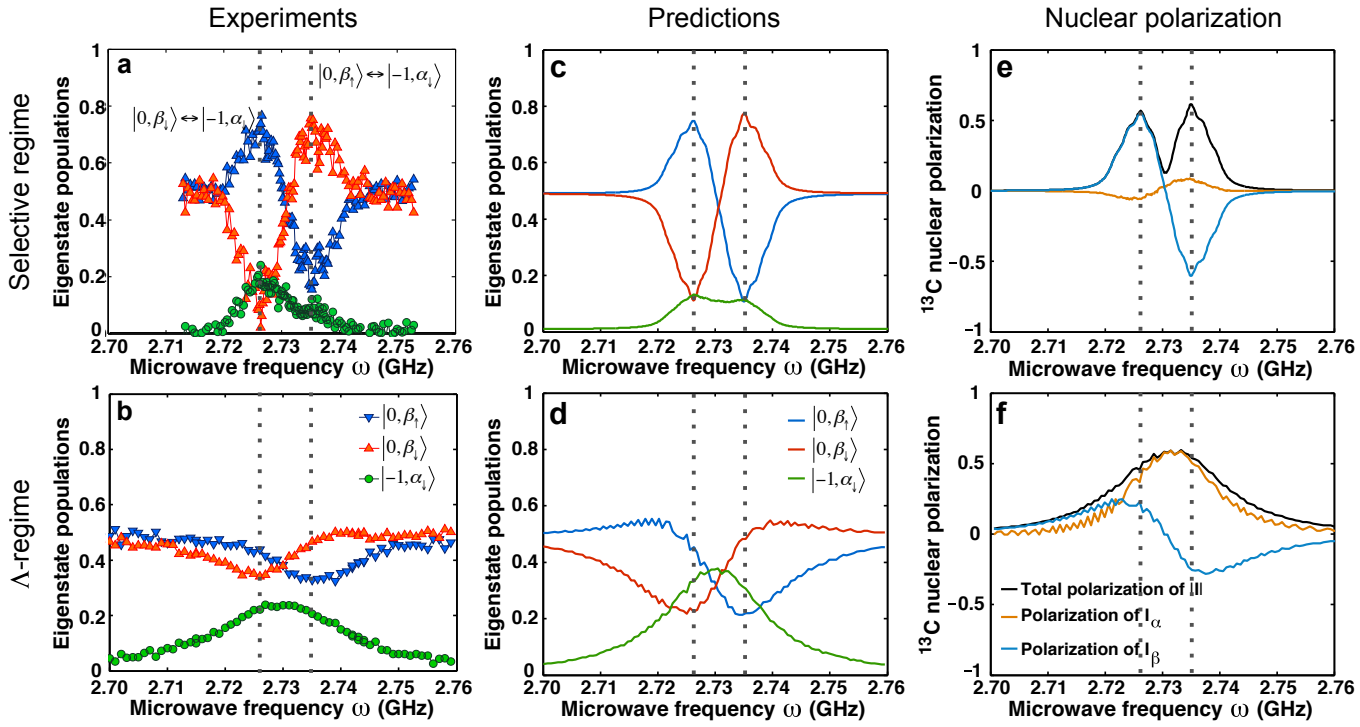

Figure 2. **Hyperpolarization of a first-shell nuclear spin using a MW-driven, optically-pumped NV center.** Experiments were done by orienting a magnetic field $|B_0| = 4.04$mT at $\theta \approx 42^\circ$ and $\phi \approx 85^\circ$ polar and azimuthal angles with respect to the zero-field tensor $\mathbf{D_0}$ of the NV center. The effective ^{13}C Larmor is then $\delta \approx 8.8$ MHz, while the first-shell hyperfine interaction is $\Delta \approx 130$ MHz. Two MW power strengths were calibrated corresponding to Rabi frequencies of $\Omega \approx 1.4\,\text{MHz} < 8.8\,\text{MHz} \approx \delta$ MHz (top panels) and $\Omega \approx 11.9\,\text{MHz} > 8.8\,\text{MHz} \approx \delta$ MHz (bottom panels), corresponding to the selective and the Λ-regime, respectively. (**a**,**b**) Optically detected experiments determining the eigenstate populations at the end of the polarization phase during 30μs as a function of the MW frequency ω. (**c**,**d**) Predicted eigenstate population spectra calculated without free parameters, i.e. using calibrated and known couplings, and a HF tensor was taken from Ref. [20]. In the selective regime (top row), the $|-1,\alpha_\downarrow\rangle$−population spectrum exhibits two peaks corresponding to the $|0,\beta_{\uparrow,\downarrow}\rangle \leftrightarrow |-1,\alpha_\downarrow\rangle$ transition frequencies, whereas in the Λ−regime (bottom row) the $|-1,\alpha_\downarrow\rangle$−population spectrum has a single peak centered half-way between the $|0,\beta_{\uparrow,\downarrow}\rangle \leftrightarrow |-1,\alpha_\downarrow\rangle$ transition frequencies. (**e**,**f**) Derived ^{13}C polarization spectra confirming the polarization directions along the $|\beta_{\downarrow,\uparrow}\rangle$-state axis (top) and the $|\alpha_\downarrow\rangle$-state axis (bottom), for the selective and Λ regimes, respectively.

larization is also reached but now aligned along an $|\alpha_\downarrow\rangle$ axis, defined by the nuclear eigenstates in the $m_s = -1$ manifold. The double peak pattern of the eigenstate population and ^{13}C polarization spectra is characteristic of the selective regime. These two ^{13}C spin alignment maxima arise when the MW is on resonance with the $|0,\beta_{\uparrow,\downarrow}\rangle \leftrightarrow |-1,\alpha_\downarrow\rangle$ transition frequencies, leading to opposite nuclear polarization directions. By contrast, in the Λ−regime, a single ^{13}C spin alignment peak centered between the $|0,\beta_{\uparrow,\downarrow}\rangle \leftrightarrow |-1,\alpha_\downarrow\rangle$ transition frequencies is observed, evidencing that these two transitions are affected by the MW, and leading to a nuclear spin alignment defined by the $|-1,\alpha_\downarrow\rangle$ nuclear quantization axis.

Bulk nuclear hyperpolarization at variable fields and orientations. The polarized NV-center is embedded in a network of dipole-dipole interacting nuclear spins, allowing an eventual propagation of the hyperpolarization throughout the nuclear bulk ensemble. Achieving an effective ^{13}C polarization enhancement throughout an entire diamond could have important practical NMR and MRI consequences. Consequently we investigated whether distant ^{13}C spins can benefit from the polarization transfer mechanisms observed in Fig. 2 at a local level. The bulk macroscopic ^{13}C magnetization was directly measured by mechanically shuttling the diamond from low fields, where MW and laser fields were applied to accomplish the electron→nuclear polarization, into a 4.7 T magnet enabling bulk ^{13}C NMR detection (Fig. 3a-b). Figure 3c presents results arising from a typical experiment, showing the dependence of the ensemble ^{13}C-magnetization on the MW frequency ω. For consistency, measurements were carried out with the polarizing B_0 field aligned along one of the NV center orientations, meaning that the remaining three orientations of the crystal form an angle of $\approx 109^\circ$ away from the field direction. The nuclear polarization spectrum (Fig. 3c) shows two regions of enhancement, corresponding to the aligned and non-aligned

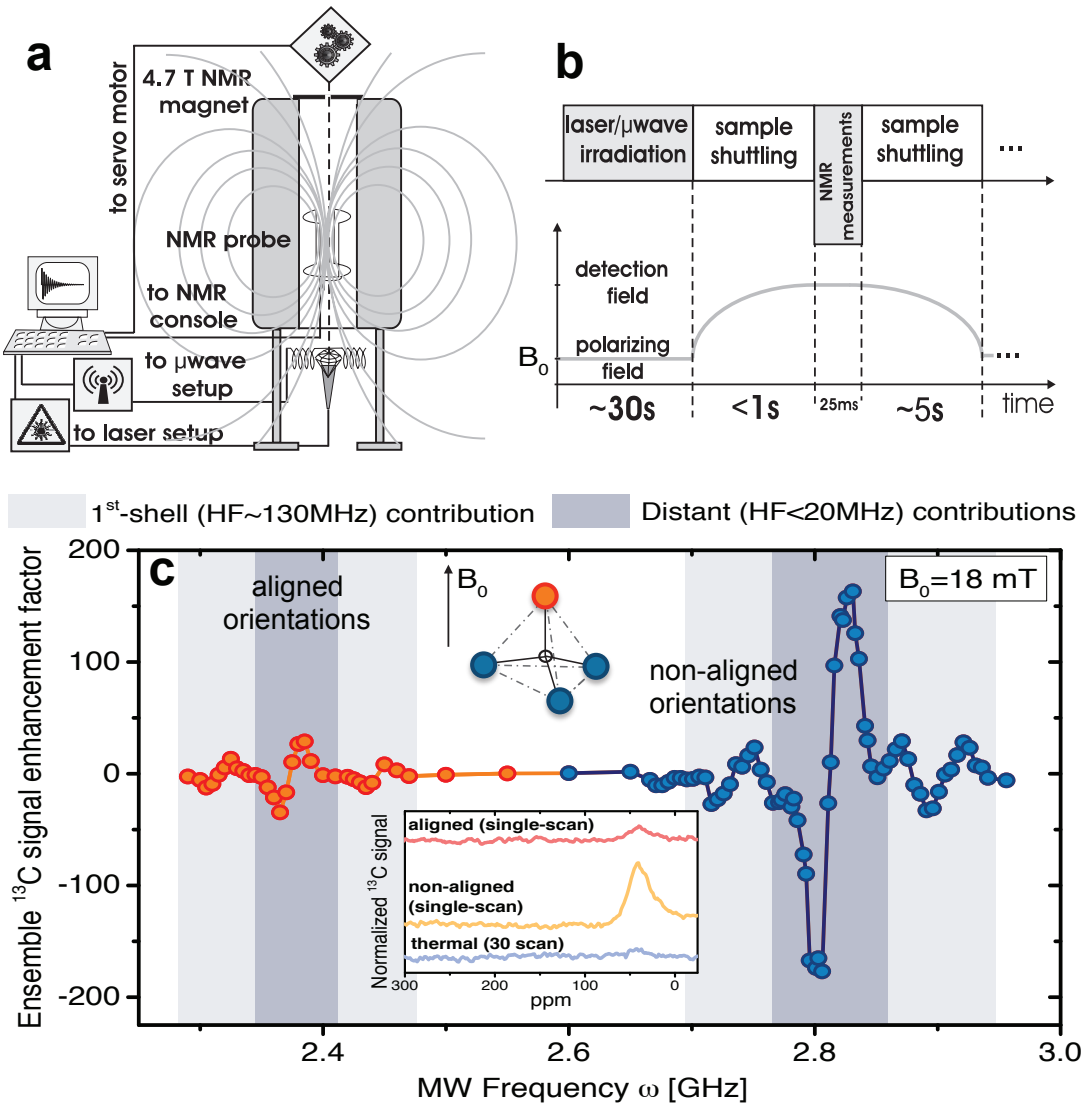

Figure 3. **Acquiring ensemble ^{13}C polarization spectra for varying NV orientations with respect to B_0.** (**a**) Opto-NMR setup and (**b**) detection sequence used in these experiments. During the polarization transfer phase, the entire single-crystal diamond is irradiated with laser light and MW underneath the NMR magnet at a low B_0. The hyperpolarized diamond is then shuttled (in <1 sec) into a 4.7 T superconducting magnet, to directly detect its macroscopic ^{13}C magnetization via a spin-echo sequence. The low B_0 magnetic field is aligned to one of the NV-center orientations (in red), while the other three orientations (in blue) subtend an angle of $\approx 109^\circ$ with respect to the field. (**c**) Typical ^{13}C polarization enhancement patterns observed by NMR as a function of the MW frequency ω with signals normalized with respect to the thermal ^{13}C response at 4.7 T (inset). The left part of the plot corresponds the nuclear polarization generated by $|m_S=0\rangle \rightarrow |m_S=-1\rangle$ MW transitions for the aligned orientation (red circles), while the right part corresponds to nuclear polarization enhanced via the three non-aligned, equivalent orientations (blue circles). The ≈1:3 intensities ratio reflects the relative abundances of aligned and non-aligned sites in the diamond's tetrahedral structure. In each of the patterns the "central" peaks represent bulk nuclear hyperpolarization pumped via ^{13}C spins coupled with HF interactions lower than 20 MHz, while the "outer" peaks originate from first-shell ^{13}C's whose HF splitting is ≈ 130 MHz [17, 20]. The "anti-phase" structure of each of these peaks corresponds to the MW transitions $|0,\beta_\downarrow\rangle \leftrightarrow |-1,\alpha_\downarrow\rangle$ and $|0,\beta_\uparrow\rangle \leftrightarrow |-1,\alpha_\downarrow\rangle$ at one side of the central peaks, and to the $|-1,\alpha_\uparrow\rangle$ state at the other side. The inset shows NMR spectra obtained for a thermally polarized sample, and at the maxima of the "central" peaks for the aligned and non-aligned orientations.

orientations of the NV defects. Both regions show similar patterns of multiple positive and negative peaks, corresponding to different HF couplings and MW-induced transitions. Both ^{13}C patterns contain major "central" peaks, and minor "outer" peaks detuned by $\approx \pm 60$ MHz from their centers. The central peaks correspond to bulk ^{13}C nuclei being hyperpolarized via $\lesssim 20$ MHz HF interactions, i.e. via ^{13}C spins positioned at or beyond the

NV's 2nd-shell [18, 19]. The outer peaks also correspond to bulk ^{13}C polarization, but arriving this time via first-shell ^{13}C's whose HF splitting is $\approx$ 130 MHz [17, 20]. In this instance the bulk ^{13}C magnetization exhibits a sign-flip pattern characteristic of the "selective" regime akin to the local ^{13}C polarization pattern shown in Fig. 2c -although these are "bulk" ^{13}C resonances detected on the whole diamond, and not "single spin" measurements. This demonstrates that ^{13}C ensemble hyperpolarization can be derived via nuclear-nuclear dipole couplings involving distant spins to the electron, but also via first-shell ^{13}C spins. The latter is a remarkable fact, given that in this case the build-up of bulk polarization needs to overcome >60 MHz detuning frequencies vis-a-vis the polarization-transfer "bridgehead". The timescales that are then needed to achieve a bulk polarization build-up, about 30 sec, are orders of magnitude longer than the first-shell electron$\rightarrow^{13}$C polarization transfer time ($\sim$ ms). This difference in timescales explains how a low-concentration, highly-detuned species like the first-shell ^{13}C, suffices to polarize the bulk sample examined by the NMR experiments. Figure 4 further demonstrates the versatility of the method to yield bulk nuclear hyperpolarization, as evidenced by the achievement of enhanced ^{13}C NMR signals over a broad range of polarizing magnetic fields and of MW powers. Notice that the nuclear polarization reveals a systematic increase as a function of B_0, as well as a clear optimum for the MW power (Fig. 4b) consistent with a transition from a selective regime in which the polarization grows with MW power, to a $\Lambda-$regime in which it decreases with the MW power (see inset).

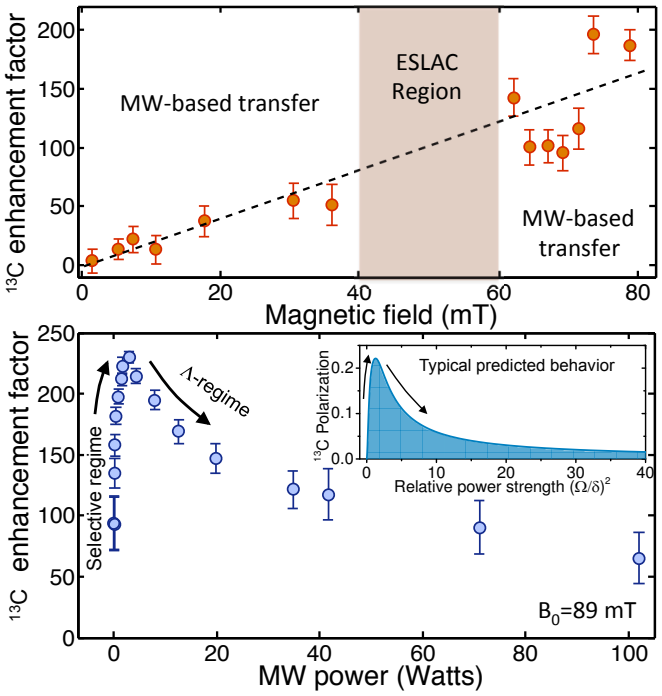

Figure 4. **Ensemble ^{13}C-magnetization for different magnetic field strengths and microwave powers.** The experimental points of these panels correspond to the maximum signal of the central peak in the aligned orientation shown in Fig. 3c. (**a**) ^{13}C polarization as a function of the magnetic field strength (normalized to its thermal 4.7 T counterpart and measured up to our maximum operating field, corresponding to $\approx$100 mT). The dashed line is a guide to the eye. Within the shaded ESLAC region [11–13] polarization transfer was observed, but such polarization transfer scheme derives from level anti-crossing and is not considered by the present model. (**b**) ^{13}C hyperpolarization as a function of the MW power at a fixed field of $\approx$ 89 mT. The inset shows the typical predicted behavior by the model, where the ^{13}C polarization grows with MW power within the selective regime, but decreases as the Λ-regime is reached.

DISCUSSIONS

A versatile method for hyperpolarizing nuclear spin ensembles at room temperature using NV centers in diamond, is proposed and demonstrated. The method relies on the combined action of continuous laser-light and microwave irradiation and exploits the asymmetries of the hyperfine interaction imparted by the $m_s = 0$ and $m_s = \pm 1$ electronic spin states. Nuclear spin hyperpolarization is obtained for a broad range of magnetic field strengths and arbitrary field orientations with respect to the diamond lattice, as well as for a wide range of hyperfine interactions. These principles may facilitate a number of applications, particularly for ensemble and nanoscale NMR/MRI [24–29], and for dissipative nuclear-state preparation of ensemble quantum memories for quantum information processing [30, 31]. They might also find applicability in other kinds of cross-polarization spin scenarios. Besides demonstrating the method's capability at a local level, it was shown that nuclear hyperpolarization can be extended throughout the bulk ensemble by spin-diffusion -even when targeting 1^{st} shell nuclear spins strongly shifted by HF couplings. This provides a new tool for understanding the complex non-equilibrium dynamics of many-body systems, where a local polarization can be created in a controlled way and its spreading into the bulk be monitored [32, 33].

METHODS

Single crystal sample. For the single NV detection experiments the sample used was a commercially available, untreated, type IIa, electronic-grade natural abundance ^{13}C diamond crystal,(dimension: 2×2×0.3 mm^3). For the NMR experiments, an isotopically enriched (10% ^{13}C) type Ib high-pressure, high-temperature (HPHT) diamonds was used. The enriched crystal was grown by the temperature gradient method at a pressure of 6 GPa

and a temperature 1700 K from Ni-2 wt.% Ti solvent using a powdered mixture of ^{13}C-enriched and natural abundance graphic carbon. These samples were irradiated at room temperature (2 MeV, 10 h, total fluence 8×10^{17} e/cm^2) and annealed (2 hours, 1000 °C). Subsequent examination by confocal laser microscopy confirmed that the two most abundant paramagnetic impurities consisted of electrically neutral single substitutional nitrogen atoms (P_1), and charged nitrogen atoms next to a lattice vacancy forming an optically active color center (NV^-). The concentrations of these impurities were both < 5 ppm.

System Hamiltonian. At room temperature the NV-center energy level structure exhibits an electronic triplet as the ground state ($^3A_2$) [11–13]. The quantum Hamiltonian of a single NV defect ($\hat{S}$) and one ^{13}C nucleus ($\hat{I}$) can thus be described as $\hat{H} = D_0\ \hat{S}_z^2 + \gamma_e\ \vec{S}\cdot\vec{B} + \gamma_e\ \vec{I}\cdot\vec{B} + \vec{I}\cdot\mathbf{A}\cdot\vec{S}$. Here $D_0 = 2.87$ GHz is the zero-field splitting term, γ_e and γ_n the electronic and nuclear gyromagnetic ratios, $\vec{B}$ is the magnetic field vector, and $\mathbf{A}$ a hyperfine tensor that depends on the specific NV and nearby ^{13}C spin. For simplicity, we consider first a magnetic field $\vec{B}$ aligned with the axis of the zero-field tensor D_0 and the secular approximation $|D_0 \pm \gamma_e B_0| \gg A_{uv}$. This Hamiltonian simplifies to $H = D_0 S_z^2 + (\gamma_e S_z + \gamma_n I_z)\, B_0 + A_{zz} S_z I_z + A_{zx} S_z I_x$, where the axis x was chosen such that $A_{zy} = 0$. The feature enabling the magnetization transfers illustrated in Fig. 1, is that in the $m_s = 0$ manifold the eigenstates have a nuclear component $|\beta_\uparrow\rangle = |\uparrow\rangle$ and $|\beta_\downarrow\rangle = |\downarrow\rangle$ exhibiting a nuclear Zeeman splitting $\delta = \gamma_n B_0$; whereas in the $m_s = -1$ manifold the $|\alpha_\uparrow\rangle$ and $|\alpha_\downarrow\rangle$ nuclear components of the eigenstates are quantized on a different axis determined by the hyperfine tensor. For the $|\beta_{\uparrow,\downarrow}\rangle$ states the eigenstate splitting δ may also depend on non-secular corrections of the HF coupling [20], which may also lead to an effective tilt of the nuclear spin quantization away from the magnetic field $\vec{B}$. By contrast, the $|\alpha_{\uparrow,\downarrow}\rangle$ states are not significantly modified by the non-secular HF terms if $|D_0 \pm \gamma_e B_0| \gg A_{uv}$, i.e. on a condition far from the level anti-crossings [12–14] (we do not consider here the more complicated scenario when the level anti-crossings conditions are fulfilled). If the magnetic field is not aligned with the $\mathbf{D_0}$ tensor, the level structure discussed in Fig. 1 remains even if the definitions of $|\beta_{\uparrow,\downarrow}\rangle$ and $|\alpha_{\uparrow,\downarrow}\rangle$ will change; the crucial characteristic is that they will still have different quantization axes and different eigenstate splittings δ and Δ.

Single NV optical setup. The single NV detection was conducted on a home-built confocal microscope. Continuous wave green laser light ($\lambda = 532$ nm) was switched by an acousto-optic modulator (Isomet, rise/fall times ≈30 ns) coupled into a single mode optical fiber and focused onto the diamond sample by an oil-immersion microscope objective (Olympus, NA=1.35). The objective was placed on a three-axis piezo stage (Npoint) enabling a scan range of the x, y, z axes of 250×250×25μm with a resolution of ∼1 nm. The emerging red fluorescence signal was focused into a single-photon counting module (Perkin-Elmer, dark count rate 100 counts/sec). To induce transitions within the ground state triplet during the polarization and detection sequences, MW fields were produced by two copper wires attached to the diamond (diameter ∼ 50 μm). During the hyperpolarization process, the laser intensity was reduced to about 5% of its saturation intensity (P_{sat} ∼1mW at the objective's back), in order to avoid light-induced nuclear-state depopulation.

Eigenstate populations and nuclear polarization determination of the single NV-center experiments. The eigenstates' populations were obtained by performing a series of complementary pulse sequences involving selective MW irradiation on eigenstate-specific transition frequencies, followed by an optical readout of the NV center populations. With these selective experiments and a linear system of equations, the populations of the three active eigenstates ($|0, \beta_{\uparrow,\downarrow}\rangle$ and $|-1, \alpha_\downarrow\rangle$) could be reconstructed. To perform these calculations, the fluorescence levels at the end of the different polarization sequences were measured, and properly normalized by executing the schemes with and without MW irradiation. In the selective regime, the MW Rabi frequency $\Omega = 1.4$ MHz was lower than the HF splitting with the ^{14}N nuclear spin (2.16 MHz). Therefore, to address the latter's three nuclear spin orientations, the MW source was further modulated to create the three corresponding frequencies spaced by 2.16 MHz. The wiggles in Fig. 2a,c,d are consequence of this irradiation mechanism. The magnetic field strength and orientation were optimized to be large enough for allowing selective excitation independent of the host ^{14}N nuclear spin ($\delta > 4-5$ MHz), and small enough to allow mutual excitation (i.e $\Lambda-$regime) with reasonable MW power ($\delta < 10$ MHz). The static and MW magnetic fields and the laser-pumping rate were calibrated from ODMR spectra, and from time-resolved measurements of the Rabi oscillations and the laser-pumping evolution. The values of the static and MW fields are given in the caption to Fig. 2, while the optical pumping rate was $1/(3\mu s)$ and had a pumping efficiency of ≈ 90%. The curves in Fig. 2c-f were obtained by solving the spins' quantum evolution based on a quantum master equation involving the total 6-level model of a single NV center coupled to a single ^{13}C nuclear spin. The bare system Hamiltonian used was introduced in the Methods section; simulations were performed on the basis of this Hamiltonian in the rotating frame of the MW irradiation, with frequency parameters as discussed in the main text. The pumping process was modeled as a non-Hermitian relaxation process using a Lindblad form reflecting the incoherent transition from

the $m_s = \pm 1$ states to the $m_s = 0$ state, using the experimentally determined pumping rate. The HF tensor of the first-shell ^{13}C spin was taken from Ref. [20]. For the selective regime, the ^{14}N HF splitting was considered phenomenologically as an ensemble superposition of the signal coming from the three frequencies used in the combed MW irradiation.

Setup for the ensemble-detected nuclear spin polarization experiments. In a single-crystal diamond, NV centers can be separated into sub-ensembles corresponding to four magnetically inequivalent orientations. The diamond sample used for the optically pumped NMR measurements had a polished [100] surface orientation. The sample was rotated in B_0 until one of the NV center orientations was aligned to the magnetic field, while the three remaining sub-ensembles were degenerate at an angle of $\sim 109°$ forming the "non-aligned" orientations. The weak magnetic field in these experiments (B_0 = 0-100 mT) was provided by the stray field of the superconducting magnet used to perform the bulk high-field NMR measurements, connected by a compensating low-field coil. The laser light was produced by a diode pumped solid-state laser (Verdi-V10, λ=532 nm) coupled into an optic fiber and then focused to either partially or fully illuminate the diamond crystals. To avoid excessive heating during the optical pumping the sample was immersed into a transparent water-filled flask and vented with pressurized air to keep the temperature constant. For the application of continuous wave MW irradiation, radio- and MW signals from a broadband frequency synthesizer were amplified by up to +30 dB for frequencies $\omega > 600$ MHz and up to +43 dB for $\omega < 600$ MHz. These amplified signals were then fed into a Helmholtz coil electronic circuit tuned to 50 Ω.

The bulk ^{13}C experiments began with a combined laser and MW irradiation ($10 - 30$ s) to optically initialize the electronic spins and induce a transfer of the ensuing hyperpolarization from the electronic to the nuclear spins. The sample was then rapidly (<0.5 s) shuttled from the polarizing field B to the "sweet spot" of the high-field (4.7 T) NMR magnet, where the nuclear spins were subject to a pulsed detection using an NMR probe with a Helmholtz coil configuration tuned to 50.55 MHz. The observed NMR signal consists of a single optically-enhanced ^{13}C spectral line resonating at ca. 60 ppm with a linewidth between 1 (natural abundance) and 3 kHz (10% enriched crystal). The sample then returned to the polarizing field for a repeated cycle of optical pumping and MW irradiation for the purpose of signal averaging.

ACKNOWLEDGMENTS

We thank Shimon Vega, Gershon Kurizki and Analia Zwick for stimulating discussions. We thank Fedor Jelezko and his group for their guiding in constructing the single NV-centers confocal microscope, and for obtaining the typeIIa sample. This work was supported by the DIP Project 710907, ERC Advanced Grant # 246754, the Kimmel Institute for Magnetic Resonance, IMOD, the Israel Science Foundation Grant 1142/13, the generosity of the Perlman Family Foundation, JST and JSPS KAKENHI (No.26246001). G.A.A. acknowledges the support of the European Commission under the Marie Curie Intra-European Fellowship for career Development Grant No. PIEF-GA-2012-328605.

AUTHOR CONTRIBUTIONS

G.A.A., R.F., and L.F. conceived the polarization transfer scheme. G.A.A., C.O.B.., R.F., P.L. and L.F. designed the experimental approaches. P.L. and R.F. implemented and performed the single spin experiments and analyzed their data. C.O.B. and R.F. implemented the hardware-setup for the bulk-NMR experiments, and G.A.A. and C.O.B. performed them, including data processing. G.A.A. and R.F. performed the numerical simulations. G.A.A., C.O.B., R.F., P.L. and L.F. analyzed and interpreted the data. H.K, S.O. and J.I. prepared the enriched diamond sample. G.A.A., C.O.B., R.F. and L.F. wrote the manuscript. All authors comment on the manuscript and contributed to discussions of its results.

* These authors contributed equally to this work.
† Lucio.Frydman@weizmann.ac.il

[1] Abragam, A. *Principles of Nuclear Magnetism* (Oxford University Press, London, 1961).
[2] Callaghan, P. T. *Principles of Nuclear Magnetic Resonance Microscopy* (Oxford University Press, 1993).
[3] Gershenfeld, N. A. & Chuang, I. L. Bulk spin-resonance quantum computation. *Science* **275**, 350–356 (1997). URL http://www.sciencemag.org/content/275/5298/350.
[4] Kane, B. E. A silicon-based nuclear spin quantum computer. *Nature (London)* **393**, 133–137 (1998).
[5] Abragam, A. & Goldman, M. Principles of dynamic nuclear polarisation. *Reports on Progress in Physics* **41**, 395–467 (1978). URL http://iopscience.iop.org/0034-4885/41/3/002/cites.
[6] Ardenkjær-Larsen, J. H. *et al.* Increase in signal-to-noise ratio of > 10,000 times in liquid-state NMR. *Proceedings of the National Academy of Sciences* **100**, 10158–10163 (2003). URL http://www.pnas.org/content/100/18/10158.
[7] Griesinger, C. *et al.* Dynamic nuclear polarization at high magnetic fields in liquids. *Progress in Nuclear Magnetic Resonance Spectroscopy* **64**, 4–28 (2012). URL http://www.sciencedirect.com/science/article/pii/S0079656511000689.

[8] Golman, K., Zandt, R. i. t. & Thaning, M. Real-time metabolic imaging. *Proceedings of the National Academy of Sciences* **103**, 11270–11275 (2006). URL http://www.pnas.org/content/103/30/11270.

[9] Joo, C.-G., Hu, K.-N., Bryant, J. A. & Griffin, R. G. In situ temperature jump high-frequency dynamic nuclear polarization experiments:??? enhanced sensitivity in liquid-state NMR spectroscopy. *J. Am. Chem. Soc.* **128**, 9428–9432 (2006). URL http://dx.doi.org/10.1021/ja0611947.

[10] King, J. P., Coles, P. J. & Reimer, J. A. Optical polarization of ^{13}C nuclei in diamond through nitrogen vacancy centers. *Phys. Rev. B* **81**, 073201 (2010). URL http://link.aps.org/doi/10.1103/PhysRevB.81.073201.

[11] Dutt, M. V. G. *et al.* Quantum register based on individual electronic and nuclear spin qubits in diamond. *Science* **316**, 1312–1316 (2007). URL http://www.sciencemag.org/cgi/doi/10.1126/science.1139831.

[12] Jacques, V. *et al.* Dynamic polarization of single nuclear spins by optical pumping of nitrogen-vacancy color centers in diamond at room temperature. *Phys. Rev. Lett.* **102**, 057403 (2009). URL http://link.aps.org/doi/10.1103/PhysRevLett.102.057403.

[13] Fischer, R. *et al.* Bulk nuclear polarization enhanced at room temperature by optical pumping. *Phys. Rev. Lett.* **111**, 057601 (2013). URL http://link.aps.org/doi/10.1103/PhysRevLett.111.057601.

[14] Wang, H.-J. *et al.* Sensitive magnetic control of ensemble nuclear spin hyperpolarization in diamond. *Nature Communications* **4** (2013). URL http://www.nature.com/ncomms/2013/130605/ncomms2930/full/ncomms2930.html.

[15] Erez, N., Gordon, G., Nest, M. & Kurizki, G. Thermodynamic control by frequent quantum measurements. *Nature* **452**, 724–727 (2008).

[16] Álvarez, G., Rao, D., Frydman, L. & Kurizki, G. Zeno and anti-zeno polarization control of spin ensembles by induced dephasing. *Phys. Rev. Lett.* **105**, 160401 (2010).

[17] Felton, S. *et al.* Hyperfine interaction in the ground state of the negatively charged nitrogen vacancy center in diamond. *Phys. Rev. B* **79**, 075203 (2009). URL http://link.aps.org/doi/10.1103/PhysRevB.79.075203.

[18] Smeltzer, B., Childress, L. & Gali, A. 13c hyperfine interactions in the nitrogen-vacancy centre in diamond. *New J. Phys.* **13**, 025021 (2011). URL http://iopscience.iop.org/1367-2630/13/2/025021.

[19] Dréau, A., Maze, J.-R., Lesik, M., Roch, J.-F. & Jacques, V. High-resolution spectroscopy of single NV defects coupled with nearby ^{13}c nuclear spins in diamond. *Phys. Rev. B* **85**, 134107 (2012). URL http://link.aps.org/doi/10.1103/PhysRevB.85.134107.

[20] Shim, J. H. *et al.* Characterization of hyperfine interaction between single electron and single nuclear spins in diamond assisted by quantum beat from the nuclear spin. *arXiv:1307.0257 [quant-ph]* (2013). URL http://arxiv.org/abs/1307.0257.

[21] Gruber, A. *et al.* Scanning confocal optical microscopy and magnetic resonance on single defect centers. *Science* **276**, 2012–2014 (1997). URL http://www.sciencemag.org/content/276/5321/2012.

[22] Jelezko, F., Gaebel, T., Popa, I., Gruber, A. & Wrachtrup, J. Observation of coherent oscillations in a single electron spin. *Phys. Rev. Lett.* **92**, 076401 (2004). URL http://link.aps.org/doi/10.1103/PhysRevLett.92.076401.

[23] Fuchs, G. D., Falk, A. L., Dobrovitski, V. V. & Awschalom, D. D. Spin coherence during optical excitation of a single nitrogen-vacancy center in diamond. *Phys. Rev. Lett.* **108**, 157602 (2012). URL http://link.aps.org/doi/10.1103/PhysRevLett.108.157602.

[24] Mamin, H. J. *et al.* Nanoscale nuclear magnetic resonance with a nitrogen-vacancy spin sensor. *Science* **339**, 557–560 (2013). URL http://www.sciencemag.org/content/339/6119/557.

[25] Staudacher, T. *et al.* Nuclear magnetic resonance spectroscopy on a (5-nanometer)3 sample volume. *Science* **339**, 561–563 (2013). URL http://www.sciencemag.org/content/339/6119/561.

[26] Loretz, M., Pezzagna, S., Meijer, J. & Degen, C. L. Nanoscale nuclear magnetic resonance with a 1.9-nm-deep nitrogen-vacancy sensor. *Appl. Phys. Lett.* **104**, 033102 (2014). URL http://scitation.aip.org/content/aip/journal/apl/104/3/10.1063/1.4862749.

[27] Abrams, D., Trusheim, M. E., Englund, D. R., Shattuck, M. D. & Meriles, C. A. Dynamic nuclear spin polarization of liquids and gases in contact with nanostructured diamond. *Nano Letters* **14**, 2471–2478 (2014). URL http://dx.doi.org/10.1021/nl500147b.

[28] Loretz, M. *et al.* Single-proton spin detection by diamond magnetometry. *Science* 1259464 (2014). URL http://www.sciencemag.org/content/early/2014/10/15/science.1259464.

[29] Sushkov, A. *et al.* Magnetic resonance detection of individual proton spins using quantum reporters. *Physical Review Letters* **113**, 197601 (2014). URL http://link.aps.org/doi/10.1103/PhysRevLett.113.197601.

[30] Verstraete, F., Wolf, M. M. & Ignacio Cirac, J. Quantum computation and quantum-state engineering driven by dissipation. *Nat Phys* **5**, 633–636 (2009). URL http://dx.doi.org/10.1038/nphys1342.

[31] Lin, Y. *et al.* Dissipative production of a maximally entangled steady state of two quantum bits. *Nature* **504**, 415–418 (2013). URL http://www.nature.com/nature/journal/vaop/ncurrent/full/nature12801.html?WT.ec_id=NATURE-20131128.

[32] Richerme, P. *et al.* Non-local propagation of correlations in quantum systems with long-range interactions. *Nature* **511**, 198–201 (2014). URL http://www.nature.com/nature/journal/v511/n7508/full/nature13450.html.

[33] Jurcevic, P. *et al.* Quasiparticle engineering and entanglement propagation in a quantum many-body system. *Nature* **511**, 202–205 (2014). URL http://www.nature.com/nature/journal/v511/n7508/full/nature13461.html.